MICROBIOLOGY

Life cycle of a cyanobacterial carboxysome

Nicholas C. Hill[1,2], Jian Wei Tay[2,3], Sabina Altus[4], David M. Bortz[4], Jeffrey C. Cameron[1,2,5]*

Carboxysomes, prototypical bacterial microcompartments (BMCs) found in cyanobacteria, are large (~1 GDa) and essential protein complexes that enhance CO_2 fixation. While carboxysome biogenesis has been elucidated, the activity dynamics, lifetime, and degradation of these structures have not been investigated, owing to the inability of tracking individual BMCs over time in vivo. We have developed a fluorescence-imaging platform to simultaneously measure carboxysome number, position, and activity over time in a growing cyanobacterial population, allowing individual carboxysomes to be clustered on the basis of activity and spatial dynamics. We have demonstrated both BMC degradation, characterized by abrupt activity loss followed by polar recruitment of the deactivated complex, and a subclass of ultraproductive carboxysomes. Together, our results reveal the BMC life cycle after biogenesis and describe the first method for measuring activity of single BMCs in vivo.

INTRODUCTION

Bacterial microcompartments (BMCs) are a widespread class of protein-based organelles found in at least 23 bacterial phyla (*1*, *2*). Composed of a protein shell encapsulating an enzymatic interior, they increase catalytic efficiency of luminal enzymes while preventing the escape of toxic or volatile intermediates into the cytoplasm. The carboxysome, an essential BMC in cyanobacteria, encapsulates the enzymes ribulose-1,5-bisphosphate carboxylase-oxygenase (RuBisCO) and carbonic anhydrase (*3*, *4*). The carboxysome functions in the CO_2 concentrating mechanism (CCM) by sequestering CO_2 in its interior, thereby maximizing RuBisCO's carboxylation rate while minimizing its oxygenation side reaction (*5*, *6*). The CCM of cyanobacteria is largely responsible for their efficient CO_2 fixation; cyanobacteria perform more than 35% of global CO_2 fixation, despite the fact that they comprise less than 0.2% of photosynthetic biomass (*7*). The efficient CCM has inspired recent efforts to incorporate carboxysomes into plants for increased crop yields (*8*, *9*).

Previous studies of cyanobacterial carboxysomes revealed that the interior is formed first through a series of protein-protein interactions, followed by encapsulation through assembly of the protein shell (*10*–*12*). However, carboxysome functionality after biogenesis, including CO_2 fixation dynamics, lifetime, and turnover, has never been analyzed. To address this problem, a method for assessing carboxysome functionality at the single protein complex level in vivo was developed. We used time-lapse fluorescence microscopy to track fluorescently labeled carboxysomes in single *Synechococcus* sp. PCC 7002 (hereafter PCC 7002) cells, chosen for their fast growth rate (*13*) and industrial relevance (*14*–*16*). Unlike bulk culture techniques, microscopy enables analysis of individual carboxysomes and has been used to describe carboxysome organization within the cell (*17*, *18*). However, previous studies were unable to assess carboxysome activity and its relation to cell growth.

Here, individual carboxysomes were tracked over 63.5 hours as they were passed from mother to daughter cells until their eventual disappearance. As wild-type (WT) PCC 7002 cells generally contain four to six carboxysomes, a system for controlling carboxysome expression was developed to minimize the number of carboxysomes in each cell. This system allows for determination of carboxysome activity; in a cell with only one carboxysome, under ambient (~0.04%) CO_2 levels, all CO_2 fixation and cell growth can be attributed to the catalytic activity of a single carboxysome, making growth rate an indicator of carboxysome activity over time.

RESULTS

To create a strain with inducible and fluorescent carboxysomes, we first incorporated a green fluorescent protein (GFP)–labeled RuBisCO (named RbcL-GFP) into the PCC 7002 genome for carboxysome visualization. The *ccm* operon, which contains the majority of carboxysome-associated genes (fig. S1A), was then knocked out, resulting in the high CO_2 requiring (HCR) Δ*ccm* strain. The *ccm* operon was then reintroduced under an isopropyl-β-D-thiogalactopyranoside (IPTG)–inducible promoter (*16*), creating the Δccm^+ strain (Fig. 1A). Segregation of all strains was confirmed via polymerase chain reaction (PCR) (fig. S1B). The Δccm^+ strain is capable of growth (fig. S1C) and carboxysome expression (fig. S1D) in ambient CO_2 only in the presence of IPTG. Cells cultured in elevated (3%) CO_2 without IPTG followed by transfer to ambient CO_2 with IPTG exhibited growth only after a lag phase, allowing for initial carboxysome formation (movie S1). The Δccm^+ strain exhibits controllable carboxysome expression and induced carboxysomes support growth characteristics identical to RbcL-GFP and WT cells (fig. S1C).

Once expected behavior of the Δccm^+ strain was confirmed, Δccm^+ cells were grown in air with 1 mM IPTG to initiate carboxysome expression. IPTG was then removed to prevent formation of new carboxysomes, and individual cells were imaged over time in ambient (~0.04%) or elevated CO_2 (3%). Family trees of representative cell lineages were created for each condition (Fig. 1, B and C). In both ambient and elevated CO_2, carboxysomes were passed from mother to daughter cell, resulting in a decrease in number of carboxysomes per cell from generation to generation. In ambient CO_2, daughter cells that did not receive a carboxysome immediately stopped growing (cells 5, 7, and 9 in Fig. 1B and movie S2), whereas daughter cells that did receive a carboxysome (cells 3, 4, 6, and 8 in Fig. 1B) continued to grow until disappearance of the carboxysome punctum (cell 8, Fig. 1B). In contrast, growth of Δccm^+ in elevated CO_2 was not dependent on the presence of carboxysomes; all cells exhibited growth regardless of carboxysome number (Fig. 1C and movie S3). These results demonstrate

[1]Department of Biochemistry, University of Colorado, Boulder, CO 80309, USA. [2]Renewable and Sustainable Energy Institute, University of Colorado, Boulder, CO 80309, USA. [3]Biofrontiers Institute, University of Colorado, Boulder, CO 80309, USA. [4]Department of Applied Mathematics, University of Colorado, Boulder, CO 80309, USA. [5]National Renewable Energy Laboratory, Golden, CO 80401, USA.
*Corresponding author. Email: jeffrey.c.cameron@colorado.edu

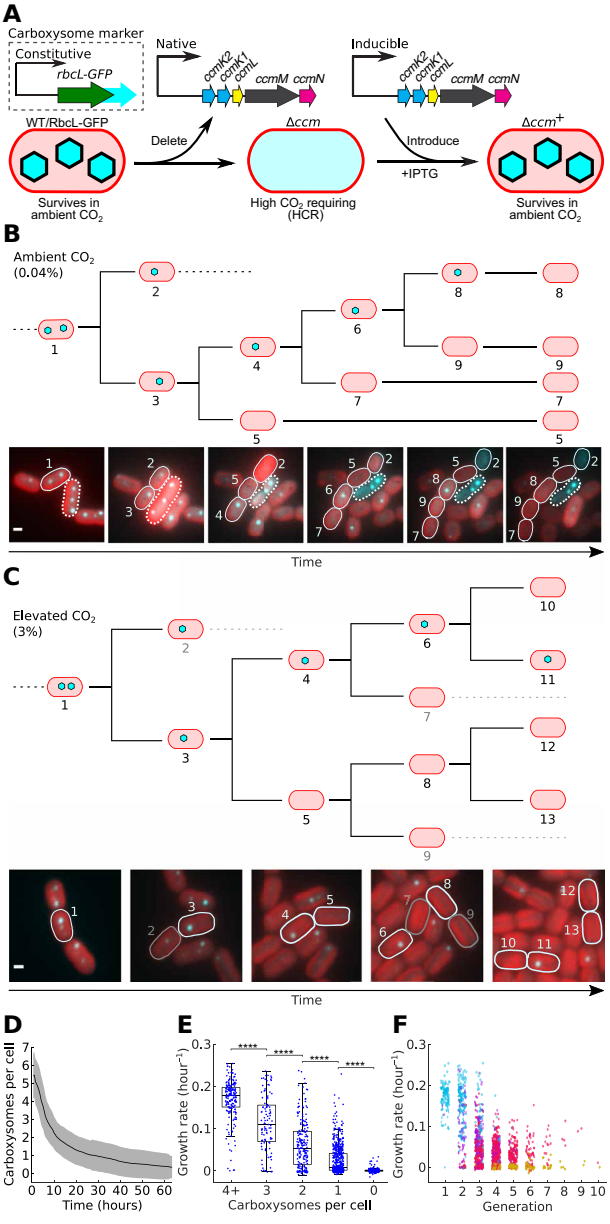

Fig. 1. Controlling carboxysome expression. (**A**) Constitutively expressed RbcL-GFP allows for RuBisCO visualization. The native *ccm* operon (*ccmK*$_2$*K*$_1$*LMN*) was knocked out, producing the HCR strain Δ*ccm*. An IPTG-inducible version of the *ccm* operon was reintroduced to create the Δ*ccm*$^+$ strain, resulting in IPTG-dependent carboxysome expression and growth rescue in ambient CO_2. (**B**) Family tree of Δ*ccm*$^+$ cells after IPTG removal in ambient CO_2. A dying cell is indicated with a dashed white outline. Carboxysomes in this cell remain static and brightly fluorescent throughout the experiment, indicating that photobleaching has a negligible effect on GFP intensity within the time span of the experiment. (**C**) Family tree of Δ*ccm*$^+$ cells after IPTG removal in elevated CO_2. (**D** to **F**) Population-level characterization of growth of the Δ*ccm*$^+$ strain upon IPTG removal in ambient CO_2. (D) Average number of carboxysomes per cell decreases as cells divide, diluting preexisting carboxysomes among the growing population. (E) Growth rate is proportional to average number of carboxysomes within a cell. $n = 191$, 108, 207, 604, and 259 for 4+, 3, 2, 1, and 0 carboxysomes, respectively. One-way analysis of variance (ANOVA) with Tukey-Kramer multiple comparison test was used for statistics (see Materials and Methods). ****$P < 0.0001$. (F) Growth rate versus generation number. Cells with 3+, 2, 1, and 0 carboxysomes are indicated in cyan, purple, red, and yellow, respectively. See fig. S3 (A to D) for colors plotted separately.

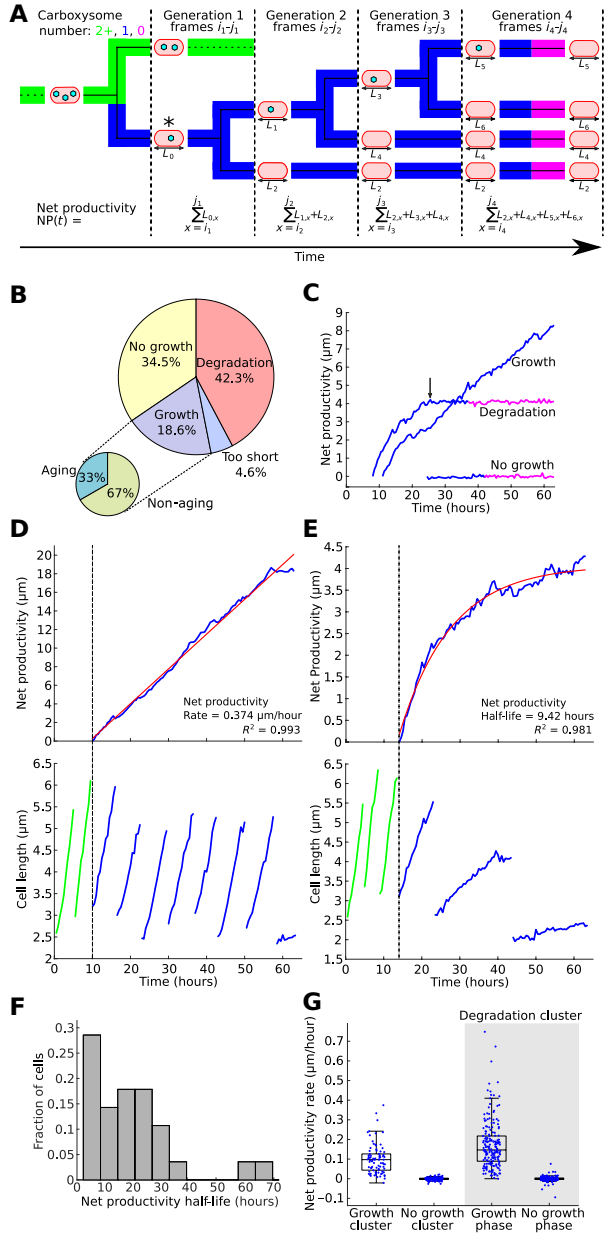

Fig. 2. Population-wide classification and activity dynamics of individual carboxysomes. (**A**) Diagram of a Δ*ccm*$^+$ family tree. The single-carboxysome tree starts at the cell indicated with an asterisk. Net productivity is calculated for each frame of the single-carboxysome tree. Green, blue, and magenta colors indicate 2+, 1, or 0 carboxysomes, respectively, present at that time in the tree. This color scheme applies in (C) to (E). (**B**) Breakdown of 452 single-carboxysome trees into clusters. The growth cluster was further split into aging and nonaging. (**C**) Net productivity traces for single-carboxysome trees in the no growth, growth, and degradation clusters. The arrow points to the frame in the degradation cluster trace that separates its growth and no-growth phases. (**D** and **E**) Net productivity (top) and cell lengths (bottom) for an ultraproductive, nonaging single-carboxysome tree (D), and an aging single-carboxysome tree (E). The cell lengths correspond only to the lineage containing the carboxysome. The dotted line indicates the first frame of the single-carboxysome tree. Linear (D) and exponential decay (E) fits for net productivity are in red. (**F**) Histogram of net productivity half-lives for all aging trees. Mean, 20.6 hours; SD, ±15.1 hours; median, 16.8 hours. (**G**) Net productivity rates for cells in the growth cluster, no-growth cluster, and the growth and no-growth phases of cells in the degradation cluster.

that growth in ambient CO_2 is dependent on the presence of at least one functional carboxysome in the cell.

Custom MATLAB scripts were used to count the number and position of GFP puncta per cell, measure single-cell growth rates based on change in cell length over time, and track individual carboxysome inheritance patterns across the population (see Materials and Methods and fig. S2, A and B). Upon IPTG removal in ambient CO_2, the number of carboxysomes per cell decreased rapidly within the growing Δccm^+ population, reaching an average of one carboxysome per cell by 26.5 hours (Fig. 1D). Growth rates correlated with the average number of carboxysomes in each cell (Fig. 1E), indicating that in ambient CO_2, cell growth is directly proportional to carboxysome-associated CO_2 fixation.

The growth rate of the Δccm^+ population gradually decreased from generation to generation, as carboxysomes were diluted across the population over time (Fig. 1F and fig. S3, A to D). As expected, all daughter cells that did not inherit a carboxysome, regardless of generation, immediately stopped growing. This sudden halt of growth indicates that alternative carbon sources, such as glycogen, are incapable of maintaining cell growth in the absence of carboxysomes.

In contrast to the Δccm^+ strain, WT and RbcL-GFP control cells maintained a high and constant growth rate over multiple generations (fig. S3, E and F). When Δccm^+ cells were grown in the presence of 1 mM IPTG, new carboxysomes were continuously produced, and multi-generational growth rates were identical to WT and RbcL-GFP cells (fig. S3G). When IPTG was removed from Δccm^+ cells grown in elevated CO_2, the growth rate remained identical to the WT and RbcL-GFP controls, despite rapid dilution of carboxysomes in the population (fig. S3H).

To further support the link between carboxysome activity and cell growth, we analyzed changes in cell size from generation to generation. Cell size was previously shown to be a function of carbon uptake in *Escherichia coli* (*19*). Similarly, cell size in PCC 7002 is regulated in response to light levels (*13*). We hypothesized that cell size would gradually decrease with increasing generation number in the Δccm^+ population, as loss of carboxysomes leads to a decreased ability to assimilate carbon. As hypothesized, length at birth gradually decreased with increasing generation number in the Δccm^+ strain in ambient CO_2 upon IPTG removal (fig. S4, A to E), whereas lengths at birth for WT, RbcL-GFP, Δccm^+ in the presence of 1 mM IPTG, and Δccm^+ in elevated CO_2 remained constant over time (fig. S4, F to J).

We then analyzed the single-cell data at single-carboxysome resolution to uncover differences in individual carboxysome activity profiles across the entire multi-generational population. The initial frame in which a cell contained one carboxysome was identified; from that frame onward, that cell and all of its descendants were grouped into a single-carboxysome tree. Cell lengths for each frame in the single-carboxysome tree were summed to obtain the length accumulation over time associated with that tree's carboxysome. Cell length provides a good proxy for biomass accumulation, as cell width remains constant in our experimental conditions. This measurement, denoted "net productivity," indicates the activity of a single carboxysome over time, as all biomass accumulation and cell growth can be attributed to a single carboxysome (Fig. 2A).

The net productivity profiles of single-carboxysome trees were clustered into four categories: "too short," "no growth," "growth," and "degradation" (Fig. 2, B and C). The too-short cluster consists of single-carboxysome trees where the carboxysome lasted less than

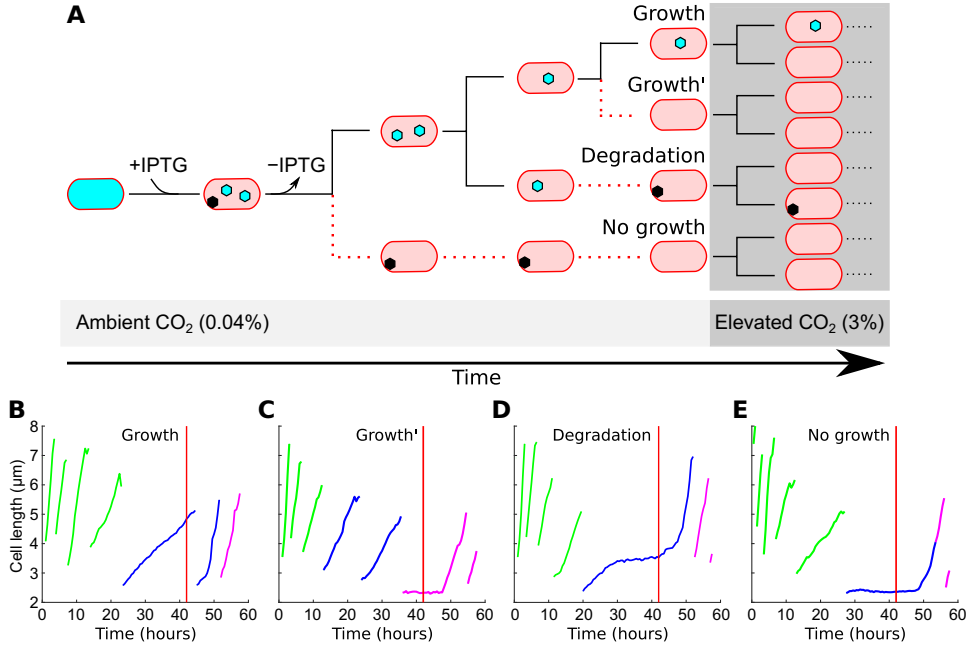

Fig. 3. Loss of carboxysome-associated CO_2 fixation is the direct cause of growth arrest. (**A**) Diagram of CO_2 rescue after IPTG removal. Cyan carboxysomes located in the cytoplasm are functional, whereas black carboxysomes located at a cell pole are nonfunctional. Red dotted lines indicate that a cell is not growing. The cluster of the single-carboxysome tree of each cell present during the CO_2 increase is indicated above the cell. The cell labeled Growth′ belongs to the growth cluster but did not inherit that single-carboxysome tree's carboxysome. (**B** to **E**) Cell lengths over time for a lineage in the growth cluster that contains (B) or does not contain (C) that single-carboxysome tree's carboxysome during the CO_2 increase. Cell lengths over time for a lineage in the degradation cluster (D) and the no-growth cluster during the CO_2 increase (E). Cell length traces in green, blue, and magenta indicate that 2+, 1, or 0 carboxysomes, respectively, are present at that time in the lineage. Vertical red lines indicate the time (42 hours) at which the CO_2 concentration was increased.

13 hours and were excluded in downstream analyses. The no-growth cluster contained nonfunctional carboxysomes that were unable to support cell growth, as seen by a constant net productivity of zero. The growth cluster contained carboxysomes that exhibited a positive net productivity rate throughout the experiment, whereas the degradation cluster was categorized on the basis of a positive net productivity rate decreasing to zero, resulting in sudden growth arrest (all clustered data in fig. S5).

There was a large degree of heterogeneity in net productivity within the growth cluster. Approximately 67% of carboxysomes within this cluster maintained a constant rate of increase in net productivity throughout the experiment and are therefore referred to as "nonaging" (Fig. 2B). One remarkable carboxysome reached a net productivity of 18 μm in less than 50 hours (Fig. 2D, top), single-handedly supporting seven generations of growth (Fig. 2D, bottom, and movie S5). The remaining third of single-carboxysome trees in the growth cluster, the

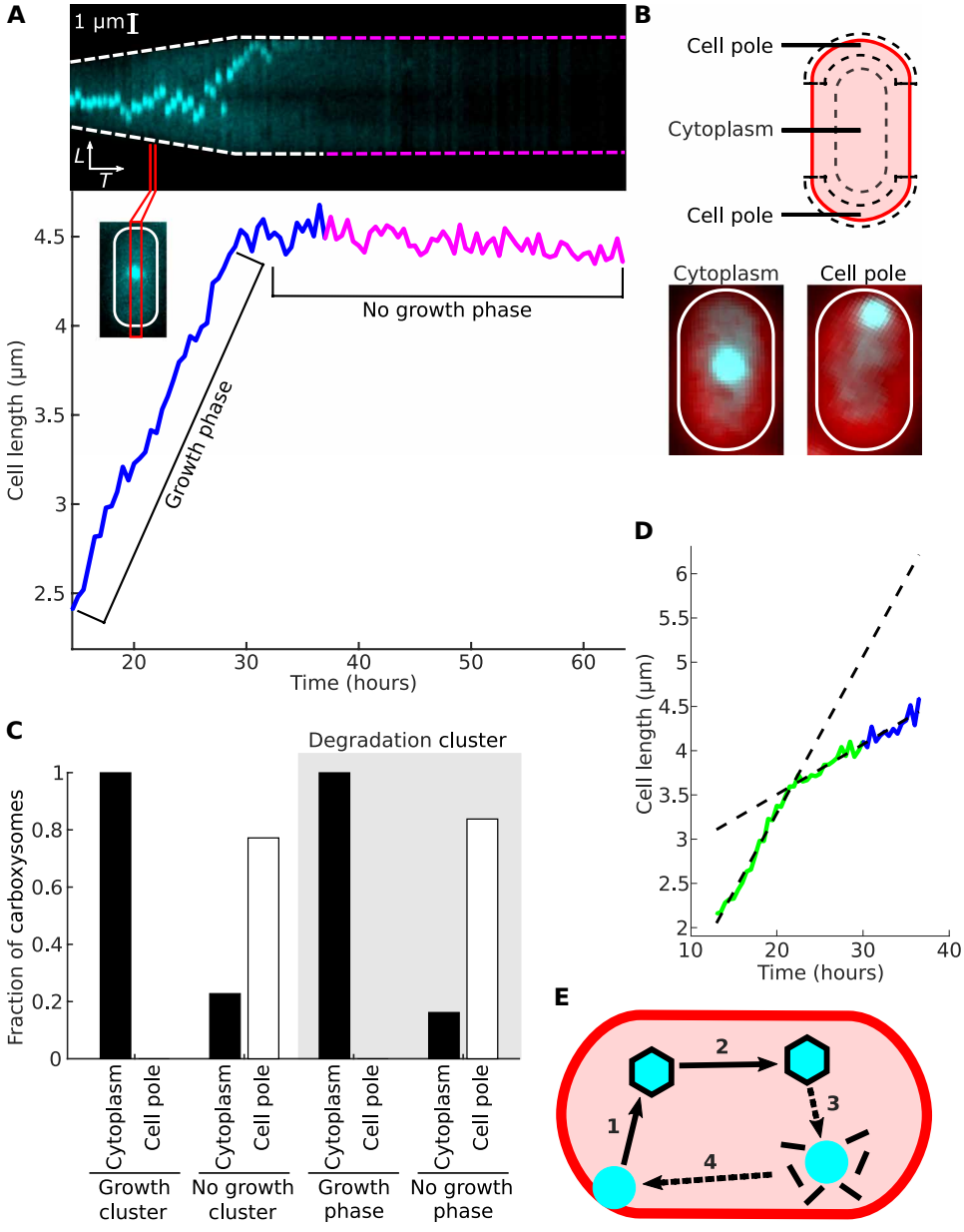

Fig. 4. RuBisCO changes localization upon carboxysome inactivation. (**A**) Kymogram (top) with corresponding trace of cell length over time (bottom); blue and magenta colors indicate 1 or 0 carboxysomes in the cell, respectively. Inset picture indicates slice of a cell shown for each time point in kymogram. Only the GFP channel (cyan) is shown. (**B**) Diagram (top) and examples (bottom) of carboxysomes localized to either the cytoplasm or a cell pole. Red, chlorophyll; cyan, GFP. (**C**) Localization of carboxysomes from different clusters ($n = 12$, growth cluster; $n = 22$, no growth cluster; $n = 31$, degradation cluster). (**D**) Cell length over time for a cell that starts with two carboxysomes (green) and ends with one (blue). Dashed lines indicate predicted growth had the carboxysome not degraded (steep dashed line) or if the cell only had one carboxysome to start with (shallow dashed line). (**E**) Model of carboxysome life cycle, including assembly of shell proteins at the pole-associated procarboxysome (1), followed by functional carboxysomes supporting many generations of cell growth (2), shell breakage/carboxysome inactivation (3), and recruitment of RuBisCO to a cell pole (4). The dashed arrow in step (3) indicates that multiple mechanisms of carboxysome inactivation could be involved, including shell breakage. The dashed arrow in step (4) indicates that RuBisCO is recruited to a pole (or developing pole at mid-cell) but may be distinct from the procarboxysome assembly intermediate.

"aging" trees, showed net productivity rates that decayed exponentially over time (Fig. 2E). Half-lives of net productivity rates for all 28 single-carboxysome trees in the aging cluster were calculated (Fig. 2F). While it is unclear why a third of single-carboxysome trees undergo this exponential decrease in activity, the half-lives are longer than the average WT doubling time (3.27 hours), indicating that even aging carboxysomes can contribute to cell growth for multiple generations.

In the degradation cluster, a sudden halt in the net productivity rate was observed, resulting in two distinct growth phases (Fig. 2C) denoted as the growth phase and the no-growth phase, as net productivity rates for each of these phases independently resemble that of the growth cluster and no-growth cluster, respectively (Fig. 2G).

To confirm that the sudden halt in cell growth observed in the degradation cluster is caused by loss of carboxysome functionality as opposed to a sudden cell death event, an identical IPTG-washout experiment was performed, but this time, the CO_2 concentration was increased from ambient (0.04%) to elevated (3%) 42 hours after IPTG washout (Fig. 3A and movie S4). Shortly after increasing the CO_2 concentration, growth of cells from the growth (Fig. 3, B and C), degradation (Fig. 3D), and no-growth (Fig. 3E) clusters was restored to WT levels. The fact that cells with either no carboxysomes or a nonfunctional carboxysome were capable of further growth and division after the CO_2 concentration increase suggests that cells enter a recoverable, quiescent-like state upon carboxysome loss and implies causation between the sudden loss of carboxysome-associated CO_2 fixation and arrested cell growth.

Loss of carboxysome activity in the degradation cluster was generally followed by a change in localization of the GFP punctum from the cytoplasm to a pole of the cell before disappearing completely (Fig. 4, A and B), highly suggestive of a carboxysome shell breakage event. Shell breakage would result in the rapid diffusion of CO_2 into the cytoplasm and abolishment of the CCM, explaining the immediate arrest in cell growth. RuBisCO's change in localization may also suggest that the carboxysome lumen is no longer distinct from the cytoplasm, as exposed RuBisCO is free to be recruited to a cell pole, where procarboxysomes (carboxysome precursors) are formed (*10*). RbcL-GFP puncta were found to change localization from the cytoplasm to a cell pole in 84% of cells in the degradation cluster (Fig. 4C). For comparison, a similar percentage of cells in the no-growth cluster contained RbcL-GFP puncta at a cell pole, while 100% of cells in the growth cluster contained carboxysomes localized to the cytoplasm (Fig. 4C).

While a subtle phenotype, it was possible to detect carboxysome degradation events in cells with two carboxysomes, as seen by a sudden decrease in growth rate followed by loss of one carboxysome (Fig. 4D). In this example, a functional CCM and expected growth rate is still maintained following carboxysome degradation, due to the presence of another functional carboxysome. This demonstrates that cells are able to distinguish between functional and nonfunctional carboxysomes and specifically target inactive carboxysomes for degradation while leaving functional carboxysomes intact.

DISCUSSION

Our study shows the continuation of the carboxysome life cycle after biogenesis and characterizes the population-level heterogeneity and activity dynamics of individual carboxysomes during CO_2 fixation. A small percentage (5%) of carboxysome in the growth cluster are considered ultraproductive, capable of supporting over 10 μm (~0.2 μm/hour), or ~5+ generations, of cell growth on their own, and should inspire future efforts aimed at maximizing carbon fixation. Our results also reveal that inactive carboxysomes are degraded, ending their life cycle (Fig. 4E).

Our results suggest that shell breakage may be the dominant mechanism of carboxysome activity loss. In an attempt to more directly visualize potential shell breakage events, we created a modified version of the Δ*ccm*$^+$ strain where the carboxysome shell protein CcmO is tagged with GFP instead of RuBisCO (Δ*ccm*$^+$_CcmO-GFP). Upon IPTG washout, carboxysomes labeled with CcmO-GFP behaved similar to the RbcL-GFP–tagged carboxysomes (movie S6). Loss of CcmO-GFP fluorescence is evident and indicates that the shell is ultimately disassembled. However, without simultaneously visualizing the carboxysome shell and its interior over time, we were unable to show that shell breakage is directly responsible for carboxysome activity loss.

If shell breakage is the primary mechanism underlying loss of carboxysome activity, then engineering efforts aimed at increasing carboxysome-catalyzed carbon fixation should focus on improving in vivo stability of the carboxysome shell in addition to improving RuBisCO catalysis. A similar degradation mechanism may also apply to other related BMCs, such as the ethanolamine utilization and propanediol utilization microcompartments (*20*). More broadly, we show the first example of measuring the long-term activity and spatiotemporal dynamics of single BMCs in vivo. We believe that this technique is well suited to assess functionality and stability of diverse BMCs, including those that increase pathogenicity in the human gut (*21*).

MATERIALS AND METHODS

Strain cultivation

PCC 7002 strains were cultivated in AL-41 L4 Environmental Chambers (Percival Scientific, Perry, IA) at 37°C under constant illumination (~150 μmol photons m^{-2} s^{-1}) by cool white fluorescent lamps, under either ambient (air, 0.04%) or elevated (3%) CO_2 conditions. Cultures were grown in 25 ml of A^+ media (*22*) in orbital shaking baffled flasks (125 ml) contained with foam stoppers (Jaece Identi-Plug), or on pH 8.2 A^+ media solidified with Bacto Agar (1%; w/v). For growth on plates in elevated CO_2, pH 11 A^+ plates were used instead. Antibiotics were added for routine growth of strains (kanamycin, 100 μg/ml; gentamycin, 30 μg/ml; spectinomycin, 100 μg/ml). Induction of the lac-controlled *ccm* operon was performed with 1 mM IPTG.

Plasmid and strain construction

All plasmids and strains used in this work are described in tables S1 and S2. Plasmids were created through Gibson assembly of plasmid backbones (pUC19 or pALM179) and PCR-amplified inserts, generated using Phusion polymerase (Thermo Fisher Scientific). Cyanobacterial strains were generated by transforming cells in exponential/early linear growth phase with 0.5 ng/ml to 2 μg/ml of plasmid DNA, containing the insert of interest flanked by 500–base pair homology arms for recombination into a specified genomic locus. After incubation at 30° to 37°C in constant illumination (50 to 150 μmol photons m^{-2} s^{-1}) for 24 hours, transformed cells were selected for with appropriate antibiotic either on plates in ambient CO_2 or in liquid A^+ in elevated CO_2, for non-HCR strains and HCR strains, respectively. From plates, individual colonies were patched onto new plates and tested for segregation. For liquid transformations, antibiotic concentration was slowly increased to up to 2× the standard concentration

over the course of a couple days. The Δ*ccm*$^+$ strain was first passaged 16× in ambient CO_2 with 5 mM IPTG to ensure complete segregation and WT growth kinetics before experimentation. Upon segregation of the culture, cells were transferred to a pH 11 A^+ plate. Confirmation of segregation was confirmed by PCR, using primers specific for either the insert, or the WT genome (fig. S1B). Presence of the insert-specific PCR product and absence of the WT-specific PCR product was used as an indicator of full segregation. All primers are listed in table S3.

Spot plating

Indicated strains in fig. S1C were grown in six-well plates in ambient CO_2 (WT, RbcL-GFP, Δ*ccm*$^+$ with 1 mM IPTG) or elevated CO_2 (Δ*ccm*). Cells were diluted to 0.05 optical density at 730 nm ($OD_{730\ nm}$) and serially diluted three times. Seven microliters of each dilution was then spotted on 1% agar A^+ plates (pH 8.2 in ambient CO_2 and pH 11 in elevated CO_2) and allowed to dry (5 to 10 min) before incubation at standard conditions noted above. When colonies appeared, spot plates were backlit on a Kaiser eVision light plate and imaged with a Nikon D7200 digital single-lens reflex camera.

Quantitative microscopy

Fluorescence images were taken using a customized Nikon TiE inverted wide-field microscope with a near-infrared–based Perfect Focus System. Temperature and CO_2 concentrations were controlled with a Lexan environmental chamber outfitted with a ProCO_2 P120 Carbon Dioxide Single Chamber Controller (BioSpherix, Parish, NY), and growth light was controlled via a transilluminating red light-emitting diode (LED) light source (Lida Light Engine, Lumencor, Beaverton, OR). A high-speed light source with custom filter sets was used for imaging (Spectra X Light Engine, Lumencor, Beaverton, OR), along with a hardware-triggered and synchronized shutter for control of imaging and growth light. NIS Elements AR software (version 5.11.00 64-bits) with Jobs acquisition upgrade was used to control the microscope. Image acquisition was performed using an ORCA-Flash4.0 V2+ Digital sCMOS camera (Hamamatsu) with a Nikon CF160 Plan Apochromat Lambda 100× oil immersion objective (1.45 numerical aperture).

For long-term time-lapse microscopy, cells in exponential or early linear phase were diluted to 0.04 to 0.07 $OD_{730\ nm}$, and 2 μl was spotted onto a 1% agarose A^+ pad that was preincubated at 37°C for 1 hour. Cells were dried onto the pad and inverted onto a 35-mm glass bottom imaging dish (ibidi), which was then wrapped in parafilm to keep the pad from drying out. No antibiotics were included on the agarose pad, but 1 mM IPTG was added when indicated. Cells were acclimated to microscope growth conditions (37°C and 150 μmol photons m^{-2} s^{-1} 640-nm light) for 30 min before acquisition of images. Images were taken every 30 min using a 470- and 640-nm LED light source (Spectra X), and emission wavelengths were collected using standard GFP and Cy5 filters (Nikon). Cells were constantly illuminated with red light except during fluorescent imaging.

Image processing and analysis

Cell segmentation

Cell segmentation was performed using MATLAB version R2017b. To segment (identify) individual cells, we also captured images in bright-field, with the focal plane offset by 2 μm. From initial testing, this offset produced the most reliable segmentation results. To remove uneven background shading, the bright-field offset image was first morphologically opened using a 30-pixel disk-shaped structuring element to obtain the background. This image was then subtracted from the original image. A Gaussian filter with an SD of 2 was then used to remove noise. Note that these images were only used for cell segmentation—reported data were measured from the original images.

Cells were then identified by applying an intensity threshold. To obtain this threshold, the intensity histogram of the background was fit to a Gaussian curve. The mean of the Gaussian plus 4 to 5.5 times its SD was then used as the threshold to create an initial mask. This initial mask often contained touching cells. To separate these cells, the watershed algorithm was used to create the final mask. Manual mask correction was then performed to correct for mistakes before data analysis.

Linking data to form tracks

After segmenting each frame, the data were linked to create *tracks* of time series data for each individual cell or object. A version of Jaqaman's tracking algorithm (*23*) was used to link data from a single object between frames followed by computation of a cost matrix. Data for each object were then assigned between frames in a manner that minimized the total cost using the Jonker-Volgenant algorithm (*24*), thus linking cell tracks.

We defined a cost function as the inverse of the ratio of the number of intersecting pixels over the total number of pixels between objects in consecutive frames. The inverse was used as the Jonker-Volgenant algorithm minimizes total cost. If required, before calculating the cost matrix, image registration was performed to correct for drifts in x and y dimensions that sometimes occurred during time-lapse experiments. After registration, the cost matrix was created by calculating costs for each object in a given frame with each object in the next frame. As PCC 7002 cells are nonmotile, a maximum linking distance was specified to avoid linking objects over physically impossible distances. Objects between frames that were separated by a distance larger than this maximum linking distance were assigned a cost of infinity. After computing all costs and assignments, some objects were left unassigned (e.g., if they were too far apart from other unlinked cells). In these instances, we checked for cell division by calculating the overlapping cost function between the unassigned object with all objects from the previous frame. If the cost fell between a set value (1 and 8), then cell division occurred and two daughter tracks were created.

Counting carboxysomes

Puncta in the GFP channel, corresponding to labeled carboxysomes, were identified by computing the difference of Gaussians (*25*) with SDs of 1.16 and 1.64 pixels. To eliminate invalid spots, only puncta brighter than 1.5 times the background were kept.

After raw carboxysome counts were calculated for each frame of every cell track for the Δ*ccm*$^+$ strain after IPTG removal in ambient CO_2, counts were corrected to increase accuracy. Raw spot counts often fluctuated slightly due to carboxysomes drifting behind one another or drifting slightly out of focus. Carboxysome counts were corrected or smoothed based on the assumption that carboxysome counts cannot increase over time within a cell track due to an inability to create new carboxysomes and the following rules. If a cell is in the first generation, set the carboxysome count of every frame to the maximum raw carboxysome count for that cell trace. If the number of carboxysomes in the first frame of a daughter cell was larger than the carboxysome count in the final frame of its mother's cell trace, then the carboxysome counts for the first two frames of the daughter

track were set to the carboxysome count of the final frame of the mother track. If the carboxysome count of a given frame is greater than the previous frame, it is set to the count of the previous frame to eliminate counting of spurious spots. If the carboxysome count of a given frame is less than the count of the previous frame and the carboxysome count of the next frame, then it is set to the carboxysome count of the previous frame to correct for spurious carboxysome disappearances. If the three frames after the current frame all have higher counts than the current frame, they are assumed to be real counts. In this case, all previous frames of the cell trace are set to the nearest integer of the average of the three frames, thus correcting the problem of a carboxysome artificially disappearing for more than one frame in a row. The reappearance of the carboxysome for three consecutive frames was considered an indication that the carboxysome was present throughout the trace, as three consecutive spurious carboxysome counts were extremely rare. Last, carboxysome counts were not allowed to decrease in the final frame of the cell trace.

Manually correcting spot counts for 82 cell traces, consisting of 3961 individual frames, showed that corrected spot counts were more accurate than raw spot counts. Raw spot counts agreed with the manually corrected spot counts 87.4% of the time, whereas the corrected spot counts agreed with the manually corrected spot counts 91.1% of the time. Many of the disagreements in the corrected spot counts come from the first 10 hours of the video, where it is most difficult to resolve 4+ carboxysomes in a single cell. As our analysis focuses mostly on cells with a single carboxysome, these inaccuracies have a minimal negative impact. The rest of the disagreements arise due to slight variations in determining the precise frame in which a carboxysome degradation event occurred, as GFP puncta gradually disappeared over time during carboxysome degradation events. Generally, the MATLAB script lost track of a carboxysome before the human eye lost track of it. As the precise timing of the complete disappearance of a GFP punctum was unimportant in our analysis, the functional accuracy of carboxysome count correcting was ~99%.

Growth rate

The growth rate of each cell track was calculated by fitting the natural log of the cell length over time to a linear polynomial (*19*)

$$\ln(L(t)) = \alpha t + \ln(L_b)$$

where $L(t)$ is the length of the cell at time t, α is the growth rate, and L_b is the length at birth. If a Δccm^+ cell contained a carboxysome degradation event that split its growth into a growth and no-growth phase, only the growth phase was used to calculate the growth rate. Note that exponential growth may not necessarily be the most accurate way to calculate growth rates of the Δccm^+ population after IPTG washout in ambient CO_2, but this analysis was used in Fig. 1 (E and F) and fig. S3 (A to D) for direct comparison with growth rates of the WT population, which does grow exponentially.

Single-carboxysome trees and net productivities

Single-carboxysome trees were defined as a subtree in a Δccm^+ family tree that only contains one carboxysome. Net productivity of the tree was calculated at each frame by adding the lengths of all cells in the tree at that time point. The length of the cell at the first frame of the single-carboxysome tree was subtracted at each time point to normalize for differences in the starting length of each tree. All biomass generated by this carboxysome before the start of the single-carboxysome tree (i.e., when it was in other cells from previous generations with more carboxysomes) is not taken into account in the net productivity calculation. For aging trees, net productivity was fit to the following exponential decay function

$$P(t) = A * (1 - e^{-t/k}) + b$$

where $P(t)$ is net productivity at time t, A is the maximum net productivity, k is the time constant, and b is the Y offset. The half-life of net productivity was then calculated by multiplying ln(2) by the time constant k.

All single-carboxysome trees were manually clustered into the growth, no-growth, and degradation clusters based on their shape. If the carboxysome lasted less than 13 hours in the single-carboxysome tree, it was instead clustered into the too-short cluster and ignored in all further analysis. Net productivity rates were calculated as the slope of the line of best fit to the data. For single-carboxysome trees in the degradation cluster, the growth phase and the no-growth phase were separated to calculate a net productivity rate for each. For aging single-carboxysome trees, the initial 10 frames were used to estimate their net productivity rates in Fig. 2G.

In Fig. 4C, the location of carboxysomes in each cluster was recorded manually. While the carboxysome position at each frame was computationally recorded, the GFP puncta often stopped being tracked in situ before it migrated to a cell pole, although it was clearly still visible by eye.

Statistics

No statistical methods were used to predetermine sample size. A one-way analysis of variance (ANOVA) with Tukey-Kramer multiple comparison test was used in Fig. 1E. F value, 646.46; total degrees of freedom, 1368.

SUPPLEMENTARY MATERIALS

Supplementary material for this article is available at http://advances.sciencemag.org/cgi/content/full/6/19/eaba1269/DC1

View/request a protocol for this paper from *Bio-protocol*.

REFERENCES AND NOTES

1. S. D. Axen, O. Erbilgin, C. A. Kerfeld, A taxonomy of bacterial microcompartment loci constructed by a novel scoring method. *PLOS Comput. Biol.* **10**, e1003898 (2014).
2. J. Jorda, D. Lopez, N. M. Wheatley, T. O. Yeates, Using comparative genomics to uncover new kinds of protein-based metabolic organelles in bacteria. *Protein Sci.* **22**, 179–195 (2013).
3. B. D. Rae, B. M. Long, M. R. Badger, G. D. Price, Functions, compositions, and evolution of the two types of carboxysomes: Polyhedral microcompartments that facilitate CO_2 fixation in cyanobacteria and some proteobacteria. *Microbiol. Mol. Biol. Rev.* **77**, 357–379 (2013).
4. A. Turmo, C. R. Gonzalez-Esquer, C. A. Kerfeld, Carboxysomes: Metabolic modules for CO_2 fixation. *FEMS Microbiol. Lett.* **364**, fnx176 (2017).
5. G. D. Price, M. R. Badger, Evidence for the role of carboxysomes in the cyanobacterial CO_2 -concentrating mechanism. *Can. J. Bot.* **69**, 963–973 (1991).
6. G. D. Price, M. R. Badger, F. J. Woodger, B. M. Long, Advances in understanding the cyanobacterial CO_2-concentrating-mechanism (CCM): Functional components, Ci transporters, diversity, genetic regulation and prospects for engineering into plants. *J. Exp. Bot.* **59**, 1441–1461 (2008).
7. M. Dworkin, S. Falkow, E. Rosenberg, K.-H. Schleifer, E. Stackebrandt, *The Prokaryotes* (Springer New York, 2006).
8. C. R. Gonzalez-Esquer, S. E. Newnham, C. A. Kerfeld, Bacterial microcompartments as metabolic modules for plant synthetic biology. *Plant J.* **87**, 66–75 (2016).
9. B. M. Long, W. Y. Hee, R. E. Sharwood, B. D. Rae, S. Kaines, Y.-L. Lim, N. D. Nguyen, B. Massey, S. Bala, S. von Caemmerer, M. R. Badger, G. D. Price, Carboxysome encapsulation of the CO_2-fixing enzyme Rubisco in tobacco chloroplasts. *Nat. Commun.* **9**, 3570 (2018).
10. J. C. Cameron, S. C. Wilson, S. L. Bernstein, C. A. Kerfeld, Biogenesis of a bacterial organelle: The carboxysome assembly pathway. *Cell* **155**, 1131–1140 (2013).

11. H. Wang, X. Yan, H. Aigner, A. Bracher, N. D. Nguyen, W. Y. Hee, B. M. Long, G. D. Price, F. U. Hartl, M. Hayer-Hartl, Rubisco condensate formation by CcmM in β-carboxysome biogenesis. *Nature* **566**, 131–135 (2019).
12. A. H. Chen, A. Robinson-Mosher, D. F. Savage, P. A. Silver, J. K. Polka, The bacterial carbon-fixing organelle is formed by shell envelopment of preassembled cargo. *PLOS ONE*. **8**, e76127 (2013).
13. H. C. Bernstein, R. S. McClure, E. A. Hill, L. M. Markillie, W. B. Chrisler, M. F. Romine, J. E. McDermott, M. C. Posewitz, D. A. Bryant, A. E. Konopka, J. K. Fredrickson, A. S. Beliaev, Unlocking the constraints of cyanobacterial productivity: Acclimations enabling ultrafast growth. *MBio* **7**, e00949–e00916 (2016).
14. A. M. Ruffing, T. J. Jensen, L. M. Strickland, Genetic tools for advancement of *Synechococcus* sp. PCC 7002 as a cyanobacterial chassis. *Microb. Cell Fact.* **15**, 190 (2016).
15. G. C. Gordon, T. C. Korosh, J. C. Cameron, A. L. Markley, M. B. Begemann, B. F. Pfleger, CRISPR interference as a titratable, *trans*-acting regulatory tool for metabolic engineering in the cyanobacterium *Synechococcus sp.* strain PCC 7002. *Metab. Eng.* **38**, 170–179 (2016).
16. A. L. Markley, M. B. Begemann, R. E. Clarke, G. C. Gordon, B. F. Pfleger, Synthetic biology toolbox for controlling gene expression in the cyanobacterium *Synechococcus sp.* strain PCC 7002. *ACS Synth. Biol.* **4**, 595–603 (2015).
17. J. S. MacCready, P. Hakim, E. J. Young, L. Hu, J. Liu, K. W. Osteryoung, A. G. Vecchiarelli, D. C. Ducat, Protein gradients on the nucleoid position the carbon-fixing organelles of cyanobacteria. *eLife* **7**, e39723 (2018).
18. D. F. Savage, B. Afonso, A. H. Chen, P. A. Silver, Spatially ordered dynamics of the bacterial carbon fixation machinery. *Science* **327**, 1258–1261 (2010).
19. M. Campos, I. V. Surovtsev, S. Kato, A. Paintdakhi, B. Beltran, S. E. Ebmeier, C. Jacobs-Wagner, A constant size extension drives bacterial cell size homeostasis. *Cell* **159**, 1433–1446 (2014).
20. C. Chowdhury, S. Sinha, S. Chun, T. O. Yeates, T. A. Bobik, Diverse bacterial microcompartment organelles. *Microbiol. Mol. Biol. Rev.* **78**, 438–468 (2014).
21. C. M. Jakobson, D. Tullman-Ercek, Dumpster diving in the gut: Bacterial microcompartments as part of a host-associated lifestyle. *PLOS Pathog.* **12**, e1005558 (2016).
22. S. E. J. Stevens Jr, C. O. Patterson, J. Myers, The production of hydrogen peroxide by blue-green algae: A survey. *J. Phycol.* **9**, 427–430 (1973).
23. K. Jaqaman, D. Loerke, M. Mettlen, H. Kuwata, S. Grinstein, S. L. Schmid, G. Danuser, Robust single-particle tracking in live-cell time-lapse sequences. *Nat. Methods* **5**, 695–702 (2008).
24. R. Jonker, A. Volgenant, A shortest augmenting path algorithm for dense and sparse linear assignment problems. *Comput. Secur.* **38**, 325–340 (1987).
25. D. G. Lowe, Object Recognition from Local Scale-Invariant Features, in *Proceedings of the Seventh IEEE International Conference on Computer Vision* (Kerkyra, Greece, 1999), vol. 2, pp. 1150–1157.

Acknowledgments: We thank B. Pfleger for providing the RbcL-GFP, Δ*ccmKLMN*::Km^R, and pALM179 plasmids. **Funding:** This study was financially supported, in part, by NIH T32-GM008759 (to N.C.H.) and by the U.S. Department of Energy (DOE) DE-SC0019306 (to J.C.C.). This research was supported, in part, by an appointment with the NSF Mathematical Sciences Graduate Internship (MSGI) program (to S.A.) sponsored by the National Science Foundation, Division of Mathematical Sciences (to D.M.B.). This program is administered by the Oak Ridge Institute for Science and Education (ORISE) through an interagency agreement between the DOE and the NSF. ORISE is managed by Oak Ridge Associated Universities (ORAU) under DOE contract number DE-SC0014664. All opinions expressed in this paper are the authors' and do not necessarily reflect the policies and views of the NSF, the ORAU/ORISE, or the DOE. **Author contributions:** J.C.C. conceived the project. J.C.C. and N.C.H. designed the study and analyzed the data with input from S.A. and D.M.B. N.C.H. generated mutant lines and performed fluorescence microscopy experiments. J.W.T. developed the tracking and segmentation algorithms with input from J.C.C. and N.C.H. N.C.H., J.W.T., and J.C.C. wrote the paper with input from all other authors. **Competing interests:** J.C.C., D.M.B., J.W.T., N.C.H., and S.A. are inventors on a patent application related to this work filed by Regents of the University of Colorado (no. 62/935,738, filed 15 November 2019). The authors declare that they have no other competing interests. **Data and materials availability:** All data needed to evaluate the conclusions in the paper are present in the paper and/or the Supplementary Materials. Additional data and MATLAB code are available from the authors upon reasonable request.

Submitted 6 November 2019
Accepted 18 February 2020
Published 6 May 2020
10.1126/sciadv.aba1269

Citation: N. C. Hill, J. W. Tay, S. Altus, D. M. Bortz, J. C. Cameron, Life cycle of a cyanobacterial carboxysome. *Sci. Adv.* **6**, eaba1269 (2020).

Science Advances

Life cycle of a cyanobacterial carboxysome

Nicholas C. Hill, Jian Wei Tay, Sabina Altus, David M. Bortz and Jeffrey C. Cameron

Sci Adv **6** (19), eaba1269.
DOI: 10.1126/sciadv.aba1269

Science Advances (ISSN 2375-2548) is published by the American Association for the Advancement of Science, 1200 New York Avenue NW, Washington, DC 20005. The title *Science Advances* is a registered trademark of AAAS.